Nanoscale

PAPER

View Article Online
View Journal | View Issue

Cite this: *Nanoscale*, 2025, **17**, 15252

Titanium diboride-derived nanosheets enhance the mechanical properties of polyurethane: experiments and simulation†

Bhagyashri Gaykwad,[a] Sree Harsha Bharadwaj H,‡[b] Archit Bahirat,‡[b] Raghavan Ranganathan[b] and Kabeer Jasuja *[a]

Received 21st March 2025,
Accepted 19th May 2025

DOI: 10.1039/d5nr01185j

rsc.li/nanoscale

AlB_2-type metal diborides have garnered significant attention in recent years owing to their ability to yield quasi-2D nanostructures. Titanium diboride (TiB_2), a key member of the metal diboride family, is well known for its extraordinary mechanical properties. However, the candidacy of TiB_2-based nanosheets to reinforce a polymer matrix has largely remained unexplored. In this work, we compare three kinds of TiB_2 reinforcements – the bulk form, pristine nanosheets, and functionalized nanosheets, with respect to their prospects in the mechanical reinforcement of polyurethane (PU). We find that while all fillers lead to an improvement in the mechanical properties of PU, the composite comprising pristine nanosheets exhibits the most significant enhancement. A 2 wt% loading of pristine nanosheets results in ~80% increase in the ultimate tensile strength and toughness. Detailed molecular dynamics simulations reveal that the TiB_2 nanosheets are not only able to distribute the load effectively, but they also promote isotropic mechanical behaviour, which makes the composite stiff and strong. These insights are supplemented by inferences from the hydrogen bonding index (HBI) and degree of phase separation (DPS). This study exemplifies the rich prospects offered by the metal diboride-derived nanosheets for reinforcing polymer matrices.

Introduction

Since the discovery of graphene in 2004, a broad spectrum of two-dimensional (2D) materials have evolved from van der Waals (vdW) layered materials.[1–4] The extraordinary intrinsic properties offered by these 2D materials have led to a number of new advances in science and technology.[5] Researchers have utilized these 2D materials in the form of stand-alone entities[6–8] as well as in the form of fillers within nanocomposites.[9,10] Several novel nanocomposites with unprecedented properties have been made possible by virtue of 2D materials and their rich diversity.[11–14] One such frontier that has garnered significant attention is wherein 2D materials are integrated within polymer matrices to reinforce their mechanical properties.[15–17] For example, the tensile strength of polyurethane (PU) can be increased by ~239% upon the addition of graphene (2 wt%)[18] and by ~80% upon the addition of boron nitride nanosheets (2 wt%).[19] Similarly, the tensile strength of nylon-6 can be improved by ~80% by adding a small fraction of functionalized molybdenum disulfide nanosheets (≤1 wt%).[20] Such extraordinary enhancements, even with a minuscule amount of nanofillers, have been attributed to the intrinsic mechanical strength of 2D materials, their high surface-to-volume ratio that enables an active interaction with the polymer matrix, and the ability of such interfaces to effectively distribute stress.[18–20]

Recent years have witnessed another important advance in the science of 2D materials, that is, strongly bonded non-van der Waals (non-vdW) layered materials can also be exfoliated into their quasi-2D counterparts. The availability of such quasi-2D nanostructures has created opportunities to create robust interfaces which were otherwise not possible. This is exemplified by MXene-based polymeric nanocomposites, where nanosheets derived from MAX phase precursors have been interfaced with several polymers.[21] The addition of MXenes has also been found to significantly enhance the mechanical properties of polymers. For instance, the tensile strength of PU increased by 47.1% after adding just 0.5 wt%

[a]*Department of Chemical Engineering, Indian Institute of Technology Gandhinagar, Palaj, Gandhinagar, Gujarat 382055, India. E-mail: kabeer@iitgn.ac.in*
[b]*Department of Materials Engineering, Indian Institute of Technology Gandhinagar, Palaj, Gandhinagar, Gujarat 382055, India*

†Electronic supplementary information (ESI) available: Information about preparation of TiB_2/PU composites. AFM images of TiB_2-based fillers. Additional characterization of TiB_2/PU composites – FESEM, TEM, DMA, XPS, FTIR, and TGA-DSC. Crystal structure of TiB_2. Mechanical properties of neat PU and TiB_2/PU composite films, equations used for simulation model construction, equilibration plots, and stress–strain curves of simulated models. See DOI: https://doi.org/10.1039/d5nr01185j

‡These authors contributed equally to this work.

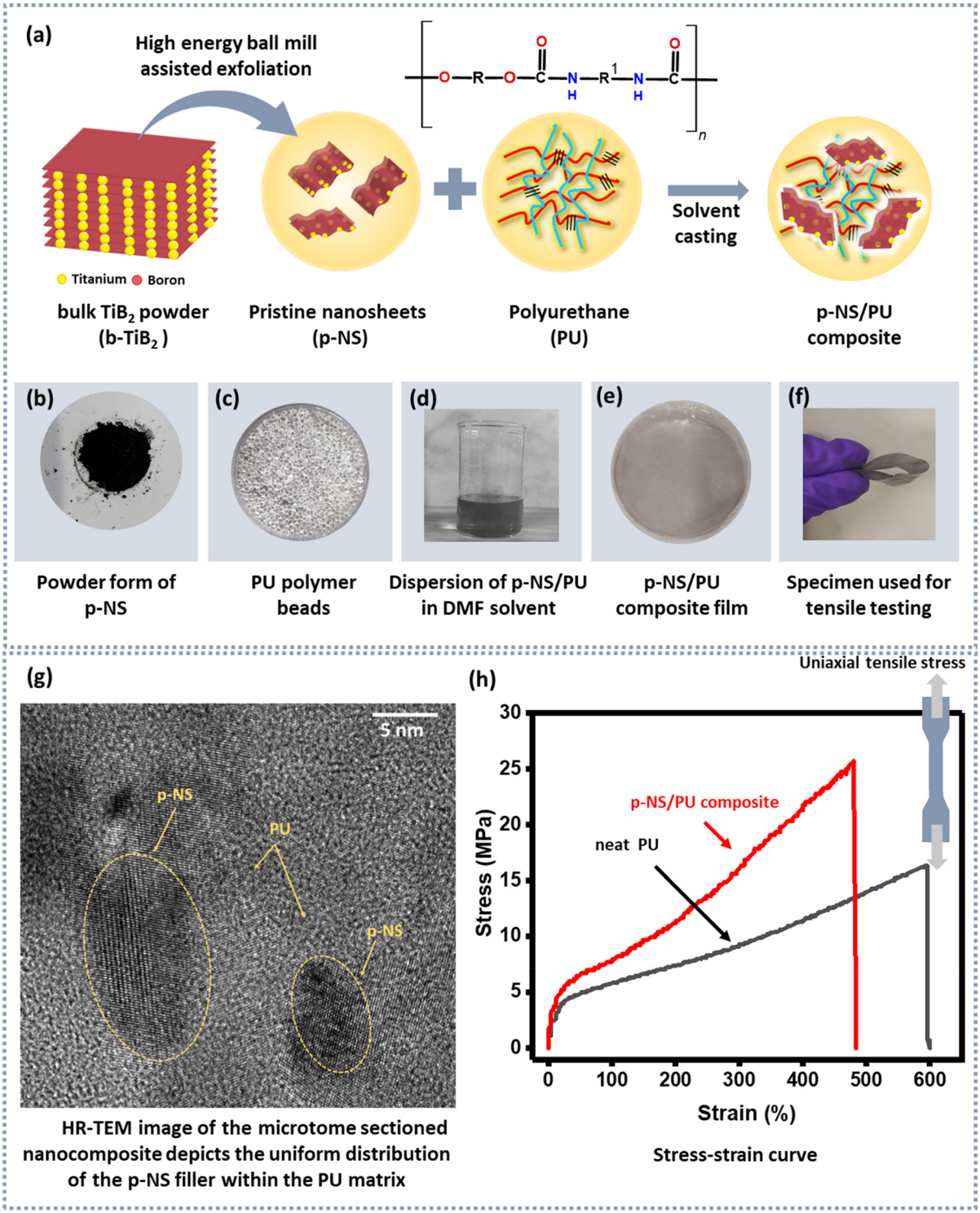

Fig. 1 Graphical representation of the preparation of TiB_2 nanosheet-based composites using a solvent casting approach. (a) Synthesis of pristine nanosheets (p-NS) using high energy ball mill-assisted mechanical exfoliation and preparation of the p-NS/PU composite film. (b) Powder form of p-NS, (c) polyurethane beads (PU), (d) dispersion of p-NS/PU in DMF solvent, (e) prepared composite film, (f) demonstration of the specimen used for tensile testing, and (g) HR-TEM image of the microtome sectioned portion of the p-NS/PU composite exhibiting well-dispersed nanosheets within the PU matrix. (h) The stress–strain curve of the neat PU film and the p-NS/PU composite indicating that the addition of p-NS significantly enhances the native mechanical properties of the PU.

MXenes.[22] Similarly, an addition of 6.7 vol% of MXenes improved the Young's modulus of poly(vinylidene fluoride) by 67%.[23] Such extraordinary enhancements indicate the rich prospects that quasi-2D materials derived from non-vdW layered materials offer in reinforcing the mechanical properties of polymer matrices.

AlB_2-type metal diborides represent one such family of non-vdW materials that have received renewed interest from the scientific community on account of their feasibility to be exfoliated into nanosheets. Such quasi-2D counterparts derived from AlB_2-type metal diborides have recently been named XBenes.[24] In the last decade, researchers have been able to exfoliate several members of this family, including MgB_2,[25–27] AlB_2,[27] TaB_2[28,29] and TiB_2,[28,30–32] into their quasi-2D counterparts. These nanosheets present a rich prospect as nano-additives for mechanical reinforcement owing to the extraordinary mechanical properties of bulk metal diborides.[33,34] Specifically, nanosheets derived from titanium diboride (TiB_2) could be potentially useful for reinforcing polymer matrices. This is because of the fact that TiB_2 itself is known for its extraordinary mechanical properties – the elastic modulus of bulk TiB_2 is ~565 GPa, which is about thirty times higher than that of graphite (15–20 MPa) and seventy times higher than that of MAX phases (2–8 MPa).[34–36] Researchers have reported that the addition of bulk TiB_2 is a promising way to enhance the stiffness of metal–matrix composites.[37–39] However, to date, there are no reports that have systematically studied the effect of nanosheets of TiB_2 as a reinforcement on the mechanical properties of polymers.

The ability to exfoliate TiB_2 in a processable dispersion has opened new avenues for the fabrication of polymer composites. To date, researchers have reported several synthesis routes to obtain nanosheets from bulk TiB_2. In 2019, Anappara and co-workers reported the synthesis of hydroxyl-functionalized nanosheets *via* shear mixing and sonication of TiB_2.[40] Subsequently, in 2020, our group reported a peroxo-based non-classical dissolution and recrystallization route to synthesize oxy-functionalized nanosheets from TiB_2.[32] In 2020, we developed a co-solvent approach for obtaining minimally functionalized nanosheets of TiB_2, where an optimal ratio of isopropanol (IPA) and water was utilized for exfoliation.[41] In 2021, Green and co-workers obtained nearly pristine nanosheets of TiB_2 by using ultrasonication in an organic solvent.[28] Recently, our group has reported the synthesis of pristine nanosheets of TiB_2 using surfactant-assisted exfoliation[31] and ball mill-assisted mechanical exfoliation.[30] The availability of such a diverse pool of TiB_2 nanosheets presents an opportunity to systematically understand the effect of interfacing quasi-2D forms of TiB_2 with a polymer.

In this study, we investigate three different kinds of TiB_2-based fillers for mechanical reinforcement of a base polymer – *bulk* TiB_2 particles (b-TiB_2), *pristine nanosheets* exfoliated from TiB_2 (p-NS), and *functionalized nanosheets* derived from TiB_2 (f-NS). We chose ball mill-assisted mechanical exfoliation[30] for synthesizing p-NS and dissolution–recrystallization[32] for synthesizing f-NS. The p-NS fillers were selected due to their retained crystal lattice structure, which remains nearly identical to that of the parent material, enabling direct comparison with b-TiB_2. In contrast, f-NS are crucial for investigating the combined effects of nanoscaling and functional groups compared with b-TiB_2.

To investigate the effect of TiB_2-based nanosheets on the mechanical properties of a polymeric system, we selected polyurethane (PU) [comprising a hard segment (di-isocyanate with chain extenders) and a soft segment (macro diol)] as the base polymer matrix (Fig. 1).[42] The rationale for selecting PU originated from its unique mechanical properties – low stiffness and strength with high ductility and toughness.[43–49]

Among all the fillers, we found that the quasi-planar nature of p-NS combined with the retained chemical integrity leads to an effective reinforcement in the PU matrix. In contrast, the presence of hydrophilic functional groups and distorted crystal lattices in f-NS limits their ability to reinforce the PU matrix. We show how the native metal boride lattice is seminal to the reinforcing ability of TiB_2 nano-additives. We also conducted molecular dynamics (MD) simulations of PU and its composites (incorporating TiB_2 nanosheets) and obtained insights that supplement these findings. In the following sections, we elucidate how these nanofillers interface with the PU matrix and result in reinforcement.

Results and discussion

To investigate the effect of TiB_2-based nanosheets on the mechanical properties of a polymeric system, we chose polyurethane (PU) as the polymer matrix. We prepared three types of TiB_2/PU composites by using the bulk form of TiB_2 and nanosheets derived from TiB_2 (p-NS and f-NS). We named these three types of composites b-TiB_2/PU, p-NS/PU, and f-NS/PU, respectively. For each of these composites, we prepared five variants by adding the fillers at 0.5, 1, 1.5, 2, and 5 wt% and compared their mechanical performance with that of the neat PU film.

We first present the structural and chemical features of these TiB_2 fillers briefly (for a detailed explanation, refer to ref. 30 and 32). Fig. 2a presents an FE-SEM micrograph of b-TiB_2 indicating thick crystals with micron-scale lateral dimensions as expected. The TEM image also supports this observation (Fig. 2d). Fig. 2b illustrates the FE-SEM micrograph of p-NS synthesized using ball mill-assisted mechanical exfoliation (as reported recently by our group).[30] This FE-SEM image depicts a planar morphology with lateral sizes in the 100–300 nm range with an aspect ratio of 25. The TEM image (Fig. 2e) and AFM images of p-NS (Fig. S1a and b in the ESI†) validate the quasi-2D nature of these nanostructures. Fig. 2c shows the FE-SEM micrograph of f-NS synthesized using dissolution and non-classical recrystallization, as reported by our group earlier.[32] This micrograph indicates >1 μm lateral size with a crumpled morphology. The TEM image (Fig. 2f) and AFM images (Fig. S1(c and d)†) also confirmed their quasi-2D nature.

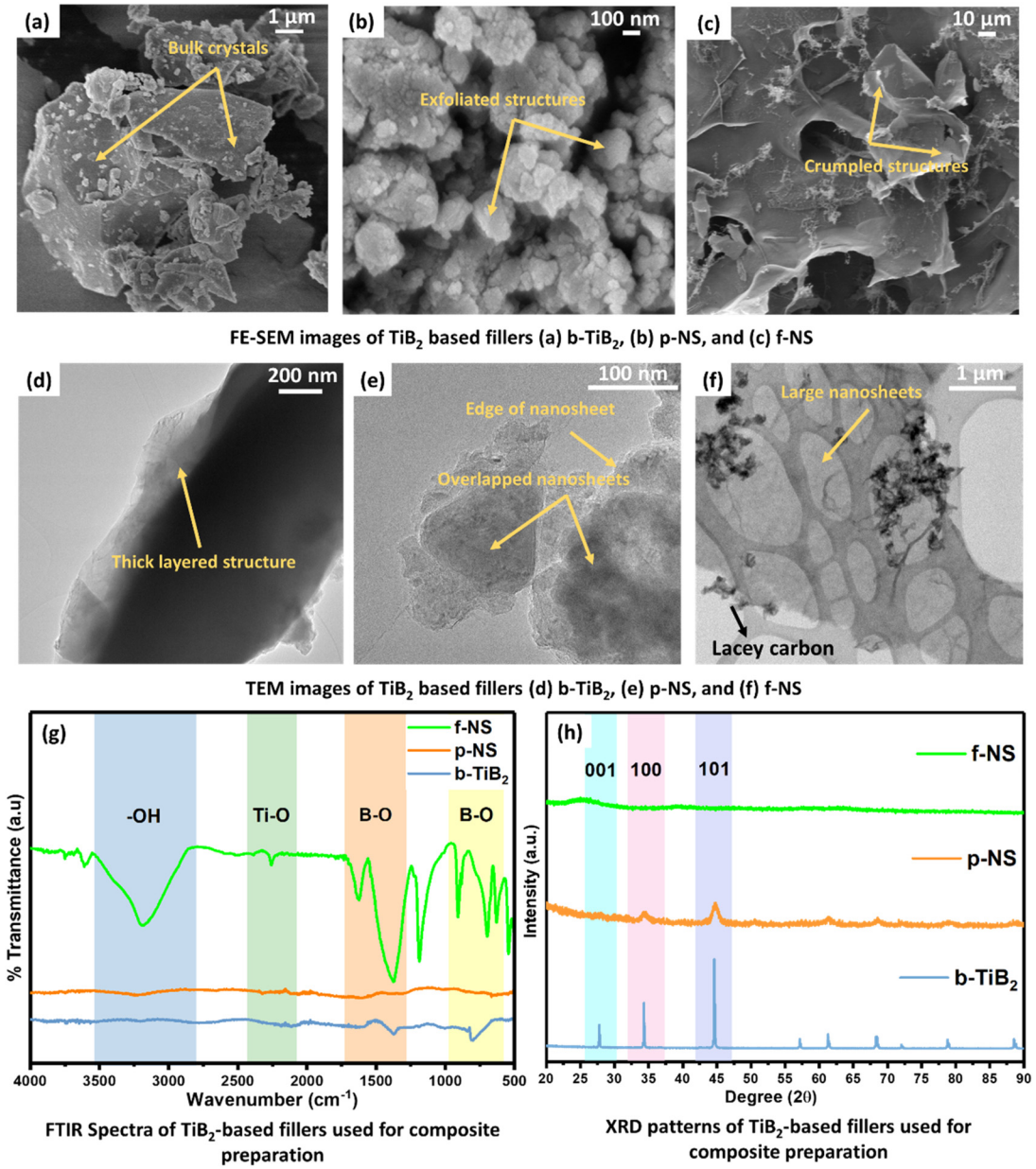

Fig. 2 Physicochemical characterization of TiB_2-based fillers. FE-SEM images of (a) bulk TiB_2 (b-TiB_2), (b) pristine nanosheets (p-NS), and (c) functionalized nanosheets (f-NS) obtained using the powder form of nanosheets, depicting substantial differences in the lateral size of nanosheets because of different synthesis methods. TEM images of (d) b-TiB_2, (e) p-NS, and (f) f-NS obtained by drop-casting the dispersion of these nanosheets on lacey carbon grids, which depict the planar nature of such nanosheets. (g) FTIR spectra of TiB_2 based fillers – b-TiB_2 and p-NS fillers, exhibiting featureless spectra, and those of f-NS indicate the extensive presence of oxy-functional groups. (h) XRD patterns of b-TiB_2 and its nanoscaled counterpart displaying the varying range of intensities. The reduction in intensity signifies that exfoliation indeed happened.

To ascertain the degree of functionalization in these TiB_2-based fillers, we recorded FTIR spectra. As shown in Fig. 2g, b-TiB_2 and p-NS exhibit almost featureless spectra, indicating minimal functionalization as expected. The FTIR spectra of f-NS indicate heavy chemical functionalization with Ti–O, B–O, and –OH functional groups. This aligns with the observation of functionalization endowed by the chemical synthesis route.[32] We performed an XRD analysis on these fillers to obtain further insights. Fig. 2h presents the XRD patterns of b-TiB_2, p-NS, and f-NS. The b-TiB_2 powder exhibits sharp peaks at 2θ values of 27.78°, 34.21°, and 44.71°, which correspond to the (001), (100), and (101) crystal planes, respectively. These peaks are in good agreement with the standard TiB_2 database (ICDD card no. 00-035-0741). The XRD pattern of p-NS also exhibits these peaks albeit with reduced intensities – this suggests that the crystallinity of TiB_2 has been retained to a large extent during exfoliation. Specifically, the reduced intensity of the peak corresponding to the (001) plane in the

p-NS XRD pattern indicates a decrease in the number of Ti and B-layers in the *c*-direction. The reduced intensities of peaks corresponding to other planes are attributed to the randomness introduced in the crystal structure during exfoliation. The XRD pattern of f-NS did not exhibit any diffraction peaks, which is in line with the heavy chemical functionalization indicating their amorphous nature.

We prepared the composites of PU with TiB_2-based fillers using the solvent casting approach (refer to Methods for a detailed procedure). To understand how the TiB_2-based fillers are distributed within the polymer matrix, we examined the morphologies of the composite films using FE-SEM and TEM. We depict the FE-SEM images of neat PU, b-TiB_2/PU, p-NS/PU, and f-NS/PU composites at 2 wt% loading. While neat PU exhibits a smooth surface with subtle spherulitic domains, PU composites comprising TiB_2-based fillers exhibit uneven surfaces with prominent spherulitic domains (Fig. S2, ESI†). Such spherulites are known to form in thermoplastics when a polymer solidifies from its melt solution.[50] TiB_2-based fillers likely act as heterogeneous nucleating agents, promoting more prominent domains. Zhang *et al.*[51] made a similar observation wherein MXenes induced heterogeneous nucleation and were centred at spherulitic domains. While these results indicate that there is a change in crystallinity upon adding TiB_2-based fillers, the DSC results indicate that the crystallinity of all the composites remains low (as explained in the section on physico-chemical insights). We also carried out HR-TEM imaging of a microtome section obtained from one of the nanocomposite films to assess if the TiB_2 nanosheets are well distributed within the PU matrix. These microtome-sectioned HR-TEM images depict that p-NS are indeed distributed within PU in a uniform manner (Fig. S3, ESI†). This is also reflected in the dynamic mechanical response of TiB_2-based composites (as explained in Fig. S4, ESI†). We have also shown the XPS survey scan of neat PU and the p-NS/PU composite in Fig. S5–S7.†

To understand how TiB_2-based fillers affect the mechanical properties of PU, we performed uniaxial tensile testing of the composites at different weight fractions – 0, 0.5, 1, 1.5, 2, and 5%. We tested at least three samples for each weight fraction for reproducibility. Fig. 3 summarizes the mechanical performance of neat PU and the composites comprising 2 wt% of TiB_2-based fillers. We selected this specific value as the composites prepared at this weight fraction demonstrated an optimal mechanical performance, as explained later. While all TiB_2-based composites exhibit higher stress values than neat PU for a given value of strain, the composites fail at a lower strain compared with neat PU (Fig. 3a).

To obtain more insights from these stress–strain curves, we determined the values of Young's modulus (Y), ultimate tensile strength (UTS), strain at break (ε_B), and toughness (T) for neat PU and each composite (refer to Table S1, ESI†). All TiB_2 based composites exhibit a higher value of Young's modulus than neat PU (Fig. 3b). While the addition of b-TiB_2 increases the Young's modulus by ~12% (23.39 MPa), the addition of p-NS and f-NS increases the Young's modulus by ~17% (24.43 MPa) and ~43% (29.81 MPa), respectively. Coleman and several other researchers have reported that a high value of Young's modulus in such 2D material-based composites is attributed to the large lateral dimensions of the fillers.[52,53] They explained that the failure mechanism of the composite depends on the functional form of the fillers. When

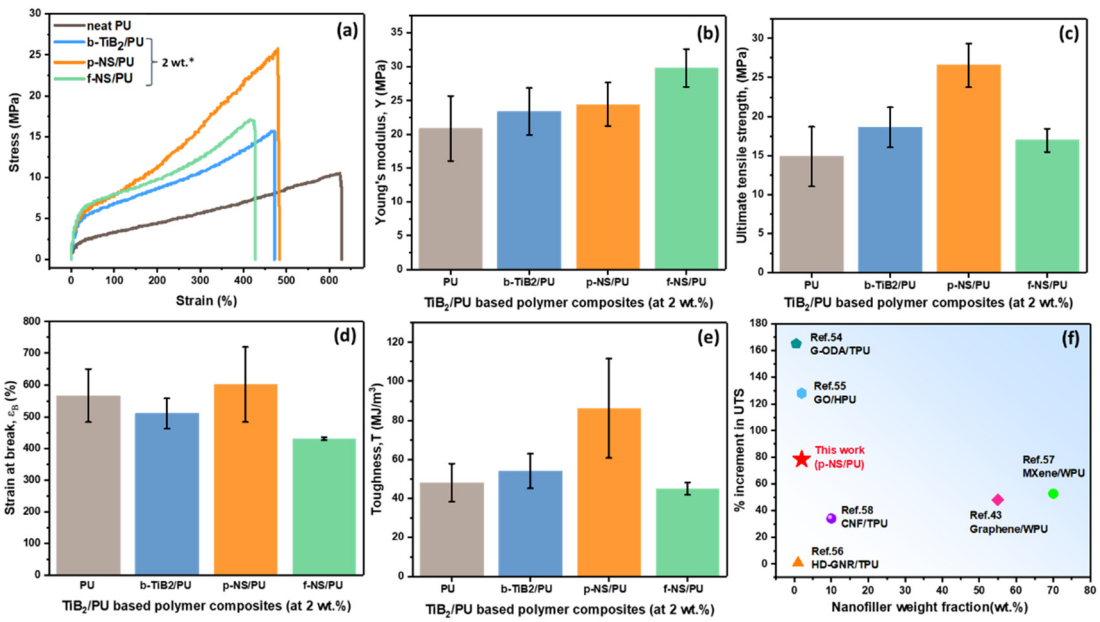

Fig. 3 Mechanical properties of neat PU and TiB_2/PU composite films. (a) Stress–strain curve. (b) Young's modulus (Y), (c) ultimate tensile strength (UTS), (d) strain at break (ε_B), and (e) toughness (T) (area under stress *vs.* strain curve) as a function of different types of TiB_2 fillers at 2 wt%. (f) Comparison of the % increment in the UTS value after adding different types of fillers in the PU matrix, in the literature and the present work.[43,54–58]

external stress is applied to a nanosheet-containing composite, some of the applied stress is transferred to the nanosheets. The intensity of stress transfer depends on the interfacial stress transfer and the aspect ratio of the nanosheets. Among all the TiB_2 fillers, f-NS exhibit the largest lateral sizes (as shown in Fig. 2c and f), which accounts for the highest values of Young's modulus for the f-NS-based composites.

All TiB_2 based composites are also found to exhibit higher values of UTS than neat PU (Fig. 3c). Among all the samples, the p-NS/PU composite exhibits the highest enhancement in the UTS value (24.43 MPa, ~80% increment compared with neat PU). The b-TiB_2 composites also show significant enhancements (~25%), albeit lower than the p-NS-based composites. This result indicates that the 3D structure of b-TiB_2 likely limits its ability to transfer stress as effectively as p-NS, the quasi-2D counterpart of b-TiB_2. This highlights the importance of nano-scaling in the context of using TiB_2-based fillers for improving mechanical properties. The f-NS/PU composite exhibits the least improvement in the UTS value among all the composites (~14% compared with neat PU). Fig. 3d exhibits the strain at break values (ε_B) for neat PU and TiB_2/PU composites. These values suggest that the p-NS/PU composite retained the native elastomeric nature of PU to a large extent. However, we observed the lowest ε_B value for f-NS/PU, which indicates that f-NS adversely affect the inherent elastomeric nature of PU and make it brittle (the probable reason for this brittleness is explained later). Toughness values also support the observation drawn from the other mechanical properties (Fig. 3e). Among all other composites, the p-NS/PU composite exhibits a maximum toughness value of 86.14 MJ m^{-3}, demonstrating an ~80% enhancement compared with neat PU.

We note that while the f-NS-based composites exhibit higher Young's modulus values than other composites, they exhibit the least improvement in other specific mechanical properties. This can be ascribed to the presence of functional groups and large lateral dimensions explained as follows. First, the native lattice of TiB_2 is heavily distorted in f-NS due to chemical synthesis, because of which the true potential of boron honeycombs, which endow the exceptional mechanical properties of TiB_2, remains untapped. Second, the hydrophilic functional groups on f-NS adversely affect the interaction with the neighbouring hydrophobic polymer. A similar phenomenon has been reported by Andronic and co-workers, where they noted that hydrophilic TiO_2 fillers get agglomerated in a hydrophobic polymer matrix, which weakens the polymer–filler interphase.[59] Lastly, we observed that when f-NS composites were stretched to their maximum limit, the composites started exhibiting microscopic voids (Fig. S8, ESI†). Such voids are not visible in b-TiB_2 and p-NS-based composites. These aspects possibly explain why f-NS-based composites exhibited a higher Young's modulus value while not showing higher values of UTS, strain at break (ε_B), and toughness, as these properties primarily represent the behaviour of the composite under loading until fracture.

The p-NS composite, on the other hand, was found to have balanced strength and ductility, resulting in an optimal increment in all specific mechanical properties. Fig. 3f summarizes some pertinent increments in UTS values from the existing literature plotted against the amount of nanofiller required for achieving the respective increments. The p-NS/PU nanocomposite investigated in this work is positioned in the middle-left region of the plot. As we can see, the TiB_2-based fillers outperform other inorganic fillers, such as MXenes, in enhancing mechanical properties. However, graphene with varying functionalization exhibits superior mechanical performance compared with TiB_2-based fillers. For the data set indicated in Fig. 3f, we have exclusively considered composites fabricated *via* the solvent casting method. For a more comprehensive comparison, we have included Table S2 in the ESI† that lists the results obtained from mechanical testing of composites fabricated using alternative approaches.

As p-NS-based composites stood out among all the TiB_2-based composites, we tested the dependence of mechanical properties of this composite on the p-NS weight fraction. Six filler fractions were chosen, namely, 0, 0.5, 1, 1.5, 2, and 5 wt%. Fig. 4a depicts the tensile response of neat PU and p-NS/PU composites as a function of the filler fraction.

To obtain deeper insights from the stress–strain curves, we investigated specific mechanical properties of the composites at various weight fractions. Fig. 4b depicts the Young's modulus values as a function of p-NS wt%. The modulus for neat PU is 20.85 MPa. It is found to increase monotonically with an increase in the filler fraction. The modulus for the 5 wt% p-NS composite is found to be 28.12 MPa, that is, ~35% higher than that for the neat PU case. These increments indicate that p-NS can significantly enhance the stiffness of PU.

Fig. 4c presents the UTS values as a function of p-NS wt%. The UTS of neat PU is found to be 14.8 MPa. It increases to 19.20 MPa upon adding a mere 0.5 wt% of p-NS (~20% enhancement) and to 26.55 MPa upon adding 2 wt% of p-NS (~80% enhancement). However, beyond 2 wt%, the UTS exhibits a decremental trend, possibly due to the aggregation of nanosheets within the PU matrix. Such an effect of agglomeration has also been shown previously by Coleman and coworkers.[43]

Fig. 4d and e show the strain at break (ε_B) and toughness, respectively. While these values do not exhibit a particular trend with increasing weight fraction of p-NS, these indicate that the composite comprising 2 wt% of p-NS exhibits optimal mechanical performance, and we can develop a stiff, strong, yet tough composite. This is the reason we selected the value of 2 wt% to compare the effect of different TiB_2-based fillers (Fig. 3). The additional datasets we obtained at other filler fractions (0, 0.5, 1, and 1.5) for b-TiB_2 and f-NS fillers are presented in Table S1, ESI.†

It is pertinent to understand how the presence of nanosheets of TiB_2 fillers endows superior mechanical properties to the PU matrix. It is known that the interphase (which is formed when fillers are added to a polymer matrix) and the inherent nature of fillers play an important role in the mechanical performance of composites.[16] We envisage a similar mechanism at play for the composites we prepared

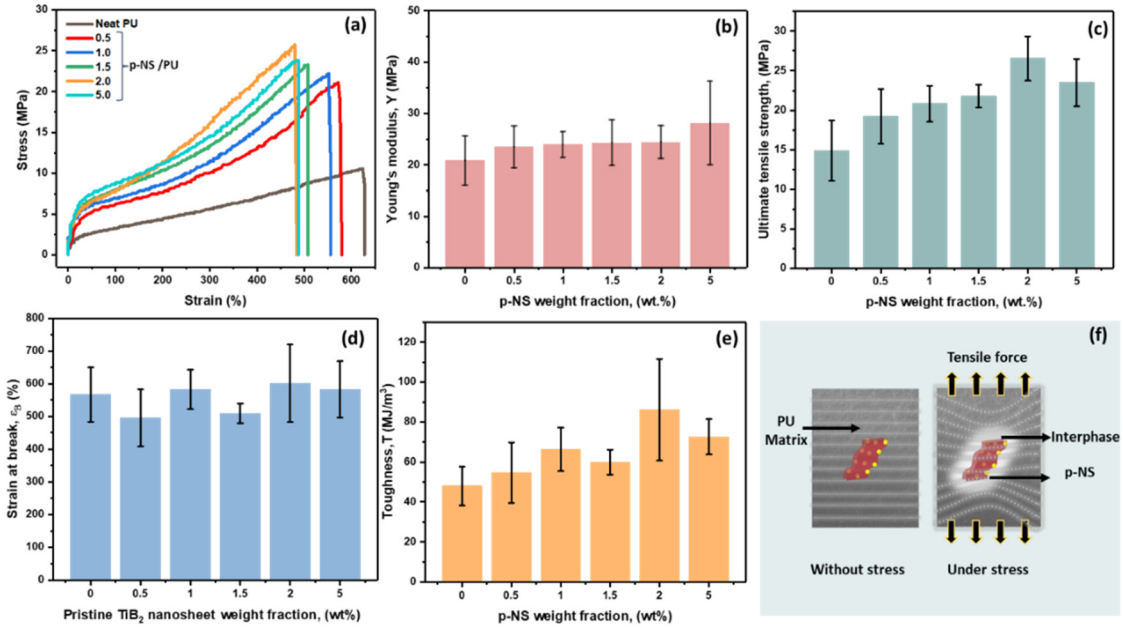

Fig. 4 Mechanical properties of neat PU and the p-NS/PU composite. (a) Stress–strain curve. (b) Young's modulus (*Y*), (c) ultimate tensile strength (UTS), (d) strain at break (ε_B), and (e) toughness (*T*) (area under stress *vs.* strain curve) as a function of the p-NS weight fraction. (f) Depiction of stress transfer at the nanosheet–polymer interphase, showcasing the changes in the deformation patterns under stress.

using TiB_2 fillers (Fig. 4f). To gain a better understanding of this phenomenon, we carried out computational studies as well as detailed physicochemical characterization. We first explain the insights obtained from simulations, and follow it up with the inferences from physicochemical studies.

Insights from molecular dynamics (MD) simulations. There are only a few computational studies available in the literature to model the structure and deformation behaviour of PUs. Rutledge and coworkers[60,61] utilized the Interphase Monte Carlo (IMC) method to model thermoplastic polyurethane (TPU) chains in their semicrystalline form and provided a foundation for correlating structural changes with macroscopic mechanical properties.[60,61] These studies revealed the mechanism behind the deformation behaviour of PU and highlighted the complex response of PU under loading conditions owing to the interplay of hard and soft segments. Notably, the enhancement of mechanical properties and interfacial deformation mechanisms for PU-based composites are poorly understood.

We developed bulk models for neat PU and four composites comprising different filler fractions of TiB_2 nanosheets (1, 2, 4, and 8 wt% of TiB_2 nanosheets) and subjected them to tensile deformation. While modelling, we modelled PU chains as amorphous because experimentally we found that the degree of crystallinity of PU and composites is very low, as explained later using DSC data.

Fig. 5a shows the equilibrated structures of PU and the composite models. The equilibrium densities of composites showed a monotonic increase with the filler fraction. For example, the density increased from 0.91 g cm^{-3} for neat PU to 1.08 g cm^{-3} for the 8% TiB_2 NS/PU composite (for details see Fig. S9 and Table S3 in the ESI†).

Fig. 5b shows the stress–strain curves obtained during tensile deformation simulations with a strain rate of 10^9 s^{-1}. For neat PU, we observed significant plastic deformation, sustaining elongation up to a strain of 7. This extensive plastic deformation can be attributed to two primary mechanisms – first, the unfolding of polymer chains and, second, their alignment and stretching along the tensile direction. We observe that the obtained value of Young's modulus of neat PU (613.6 MPa) is lower than the values reported by Zhu *et al.*[61] for semicrystalline PU and by Talapatra *et al.*[62] who reported a modulus of 0.98 GPa for neat amorphous PU. We also note that the modulus calculated from our MD simulations is an order of magnitude higher than our experimental values owing to several well-known reasons, such as the choice of the interatomic potentials, the representative model structures themselves (smaller chain lengths and different chain chemistries) and much higher strain rates than that of experiments (due to the limitations in terms of timescales that can be simulated using MD).[63] Notwithstanding these limitations, MD offers a powerful means to understand the reinforcement mechanisms. The Young's modulus for composites calculated from MD simulations showed a consistent increase with higher TiB_2-NS weight fractions, indicating improved stiffness in the composites (refer to the inset in Fig. 5b). This trend is consistent with our experimental findings. With higher TiB_2-NS weight fractions, the PU polymers adhering to the surface of TiB_2 nanosheets undergo unfolding and stretching, leading to void formation near the nanosheets. This behaviour is attribu-

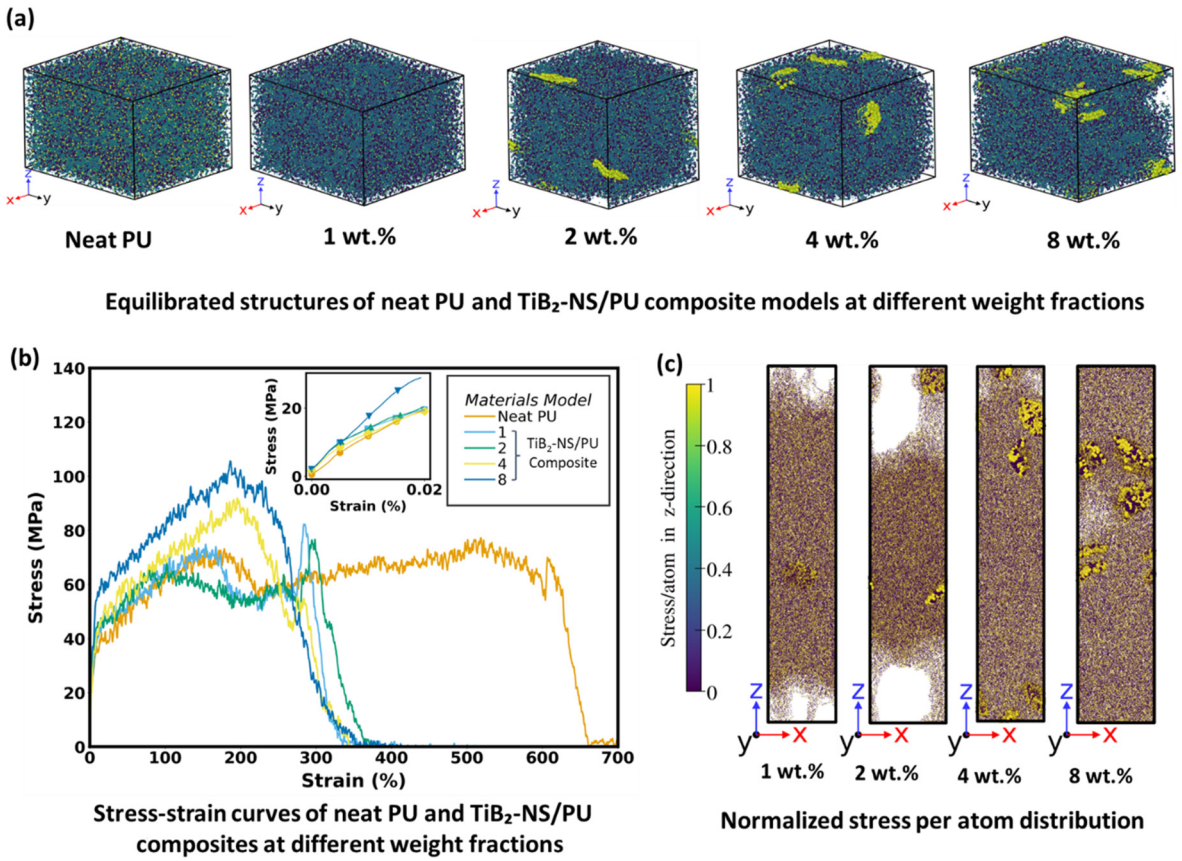

Fig. 5 MD simulations of neat PU and composites of different weight fractions. (a) Equilibrated structures of PU and composites models (1, 2, 4 and 8 wt% TiB_2-NS), (b) stress–strain curves of neat PU and composites as a function of the TiB_2-NS weight fraction, and (c) stress per atom distribution in TiB_2-NS/PU composites along the *z*-direction at a strain of 3.

ted to the weak Lennard-Jones (LJ) potential at the polymer–TiB_2 interface. Despite the distortion of TiB_2 nanosheets during deformation, they contribute significantly to the reinforcement of the composite, as highlighted in Fig. 5b. Furthermore, as the TiB_2 content increases, the strain at which failure occurs decreases, indicating reduced ductility. However, this is accompanied by a notable increase in Young's modulus and yield strength, emphasizing the trade-off between stiffness and elongation at break in these composites, in accordance with our experimental observations. The mechanical properties for all the modeled structures are summarized in Table S3.† These simulated results are also in accordance with our experimental results. It is to be noted that there are quantitative differences with respect to our experimental measurements due to the aforementioned factors in the simulations; however, the trends for the mechanical behavior agree quite well with experiments.

In Fig. 5c, we show how the stress per atom is distributed for the various structures at a strain of 3. The colour bar represents the magnitude of stress per atom on a scale of 0 to 1. This shows that TiB_2 nanosheets actively take part in stress distribution, an essential requirement for enhancement of mechanical properties. For more insights, we captured the snapshots of the deformation at a strain of 3 for neat PU, 4 wt%, and 8 wt% TiB_2-NS/PU composites (Fig. S10, ESI†). These snapshots provide visual evidence of the changes induced by TiB_2 nanosheets in the PU matrix. We observed that the neat PU depicts a highly anisotropic deformation behaviour (see Fig. S10, ESI†). At the strain of 3, the cavitation occurs only in one direction (along the *y*-axis), while elongation continues along the *x*- and *z*-directions. This indicates that the orientation of the hard and soft segments has a strong role in load-bearing during extension. However, this effect is expected to be much less in our experimental samples. For TiB_2-NS/PU composites, the anisotropy decreased significantly with increasing TiB_2-NS weight fractions due to the presence of the fillers and the ensuing interfacial interactions with PU. We also note that varying the aspect ratio of the TiB_2-NS offers further scope for optimization of the mechanical properties.

Physicochemical characterization. To gather deeper insights into the interphase formed between the fillers and the polymer matrix and to quantify the nature of polymer/filler interactions, we recorded the FTIR spectra of neat PU and composites (Fig. 6a). The FTIR spectra of neat PU exhibit five primary bands – 3330 cm^{-1} (hydrogen-bonded N–H stretching vibration), 2959 cm^{-1} (asymmetric CH_2 stretching), 1729 cm^{-1}

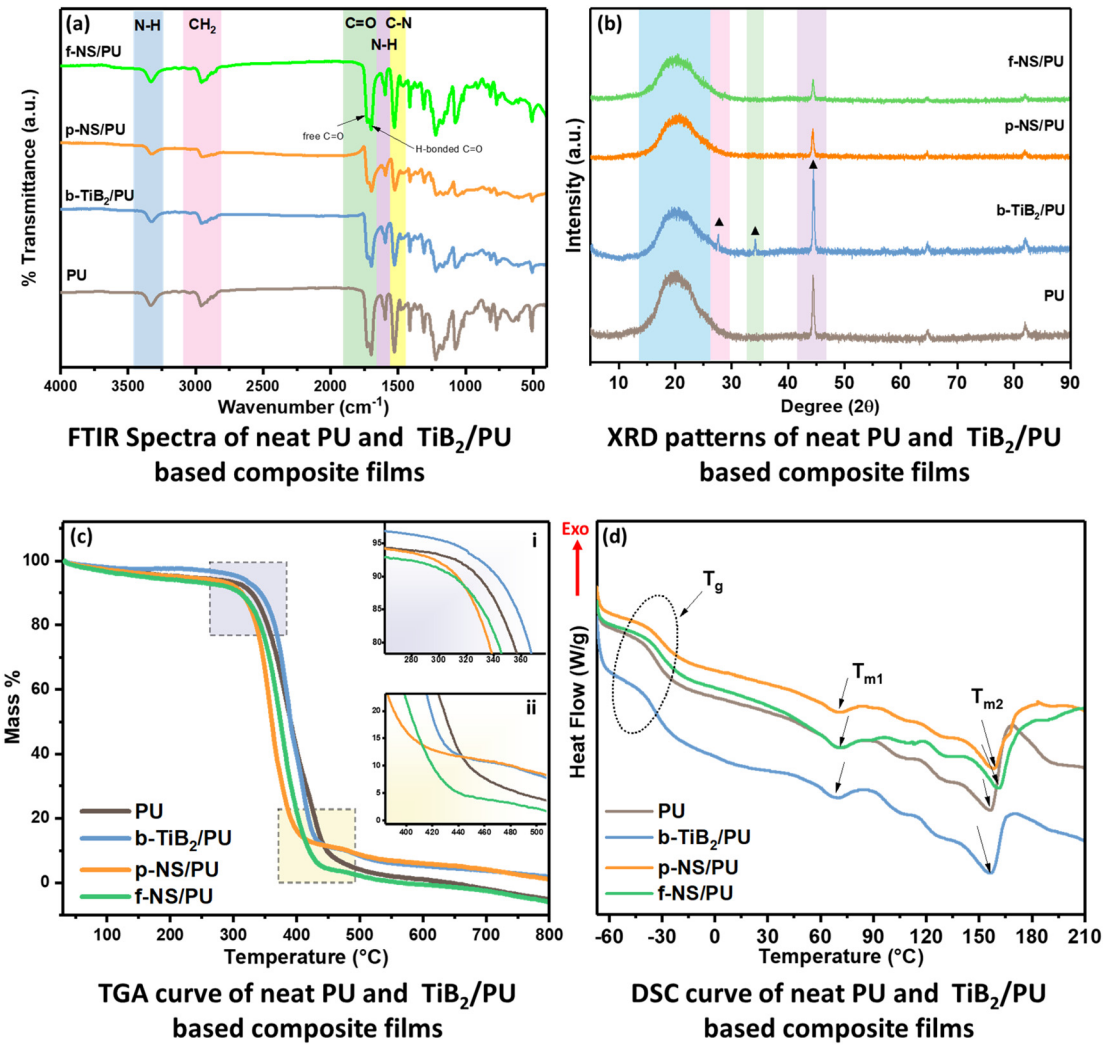

Fig. 6 Chemical and thermal characterization of neat PU and its composites at 2 wt% addition of TiB_2 based fillers. (a) FTIR spectra depict a reduction in intensity for b-TiB_2 and p-NS-based composites compared with neat PU, reflecting an interaction between these fillers and PU, which is not evident in an f-NS-based composite. (b) XRD patterns exhibit no significant change in the crystal structure of native PU; (c) TGA and (d) DSC curves also demonstrate the changes in the thermal characteristics of composites compared with neat PU, representing an interaction between TiB_2-based fillers and PU.

(stretching vibration of free carbonyl group), 1699 cm^{-1} (stretching vibration of the H-bonded carbonyl group), and 1526 cm^{-1} (C–N stretching). Compared with neat PU, we observed a gradual decrease in the intensity of the bands for b-TiB_2/PU and p-NS/PU composites (refer to Table S4, ESI†). This decremental trend of the b-TiB_2/PU and p-NS/PU composites indicates that these fillers chemically interact with the PU matrix.[54,64] However, for f-NS/PU composites, we observed no significant change in the intensity compared with neat PU, which suggests that f-NS do not interact well with the PU matrix. This also explains the decrease in the mechanical performance of the f-NS-based composite compared with other TiB_2 composites. However, one recent report exhibits that these f-NS interacted well with a biopolymer,[65] but the studied polymer was hydrophilic in nature. This underscores the importance of considering the wetting characteristics of both fillers and the polymer during composite preparation.

To quantify the degree of interaction, we chose the carbonyl stretching region (1672–1761 cm^{-1}). This region indicates the formation of hydrogen bonds between hard segments. We calculated the hydrogen bonding index (HBI) and the degree of phase separation (DPS). To calculate HBI values, we measured the intensity ratio of the H-bonded carbonyl band to the free carbonyl band. The method to calculate the HBI and DPS is presented in the ESI under Section S12.†

The HBI values, as shown in Table 1, were obtained using the carbonyl region as shown in Fig. S11 in the ESI.† We note that for b-TiB_2 and p-NS filler-based composites, the HBI value was slightly reduced. This suggests that such fillers might be non-covalently attached to the PU matrix and hence restrict

Table 1 Calculation of the hydrogen bonding index (HBI) and the degree of phase separation (DPS)

Samples	I_{1699}	I_{1730}	HBI	A_{1699}	A_{1730}	DPS
Neat PU	36.61	43.71	83.76	13.51	18.41	0.73
b-TiB_2/PU	26.28	33.58	78.26	11.37	17.9	0.64
p-NS/PU	20.25	27.77	72.92	11.53	17.11	0.67
f-NS/PU	34.72	41.22	84.23	13.28	18.87	0.70

the motion of the hard segment.[66] The composites also exhibit slightly lower DPS values than neat PU, which indicates that these fillers hinder the phase separation of hard and soft segments. Additionally, we did not observe any new band for composites, which signifies the well-distributed fillers in the polymer matrix.

To obtain some physical insights, we studied the cross-sectional FE-SEM images of the fractured surface of neat PU and TiB_2/PU composites (Fig. S12 and S13†). The FE-SEM image of the neat PU film depicts a smooth surface without any fractures (Fig. S12a†). In contrast, the FE-SEM images of composites show rough surfaces. Particularly, the fractured surface of b-TiB_2/PU and p-NS/PU composites depicts a small number of fillers on the surface (as shown in Fig. S12b and c†), which indicates a strong interaction of these fillers with the polymer. However, we observed several nanosheets protruding outwards in the case of the f-NS/PU composite, which indicates a weaker interaction of f-NS with PU (Fig. S12d†). Tensile testing and FTIR results also corroborate these inferences.

We also investigated the changes in crystal structures in the PU matrix after incorporating TiB_2-based fillers. Fig. 6b shows the XRD patterns of neat PU and its composites. The neat PU exhibits primarily two peaks at 19.98° and 44.38°. The first peak represents the short-range ordered structure of hard and soft segments,[67,68] and the second peak represents the oriented hard domains. TiB_2/PU composites exhibit a reduction in the first peak with respect to neat PU. This is due to the interaction between the polymer and the filler, which disrupts the typical molecular arrangement of PU. Moreover, specifically, in the b-TiB_2/PU composite, two new peaks emerge at 27.67° and 33.97°, which indicates the presence of (001) and (100) planes of b-TiB_2 (shown by a triangle in Fig. 6b). The possible reason behind the emergence of these peaks in b-TiB_2/PU composites is the highly crystalline structure of b-TiB_2, as shown in the XRD pattern (Fig. 2h). Moreover, there is an increment in the intensity of the 44.38° peak due to an overlapping of the (101) peak of b-TiB_2. We did not observe any new peak in the case of p-NS and f-NS-based composites because of their weak crystallinity compared with b-TiB_2 (as shown in XRD patterns, Fig. 2h).

To obtain insights into the strength of the bonds between fillers and matrix, we performed TGA-DSC analysis on neat PU and the TiB_2/PU composite. Fig. 6c shows the TGA curve of neat PU and the composite films at 2 wt% loading. As shown, neat PU and its composites exhibit a two-stage decomposition behaviour. The first stage ranges from 283 °C to 440 °C, which occurs due to urethane bond decomposition. The second stage is between 450 °C and 653 °C, which occurs due to the decomposition of the polyol segment and thermo-oxidative degradation of the polyurethane backbone. We measured the temperature at 10% and 90% weight loss of the initial sample, representative of the changes in both decomposition stages, as shown in Table S5, ESI.† For b-TiB_2/PU composites, we observed a significant temperature shift compared with neat PU. For instance, the temperature for 10% weight loss ($T_{10\%}$) is shifted from 328 °C to 342 °C, and the temperature for 90% weight loss ($T_{90\%}$) is shifted from 448 °C to 482 °C. This temperature shift indicates that b-TiB_2 particles likely delay the decomposition of PU bonds. For p-NS/PU composites, we observed no shift for 10% weight loss ($T_{10\%}$), and a significant shift in the $T_{90\%}$ (shifted from 448 °C to 482 °C). This temperature shift is similar to that for b-TiB_2-based composites and is ascribed to the fact that b-TiB_2 and p-NS fillers restrict the motion of the polymer. Thakur *et al.* found that the restrictive motion of polymer chains can be attributed to robust physicochemical interactions between the filler and the polymer.[55] In contrast, f-NS/PU composites exhibit a negative shift in temperature compared with neat PU at both weight loss percentage. This observation confirms the lack of interaction between f-NS and neat PU, which is consistent with the FTIR and tensile testing results. The increase in the residual amount at 600 °C also indicates that the addition of b-TiB_2 and p-NS improves not only the mechanical properties but also the thermal properties.

Furthermore, we used DSC to gather insights into the changes in the melting and crystallization behaviour because this is also influenced by the interaction of these TiB_2-based fillers with PU. In Fig. 6d, we have shown the DSC thermograms of neat PU and TiB_2/PU composites. We determined the glass transition temperature (T_g) and melting temperature (T_m) of neat PU and its composites from DSC thermograms, as shown in Table S6 in the ESI.† It is visible that the T_g values of p-NS and f-NS-based composites increased in comparison with neat PU. However, for b-TiB_2-based composites, the T_g remains the same, likely due to the agglomeration of b-TiB_2 fillers at the T_g, facilitating an easier movement of polymer chains. Unlike b-TiB_2, the decrement in the T_g values of p-NS and f-NS-based composites suggests reduced molecular motion of PU chains due to these fillers. Moreover, we observed two melting endotherms –T_{m1} and T_{m2} in neat PU and composites. We observed no significant change in the T_{m1} value, as shown in Table S6, ESI.† However, we observed a significant incremental change in the T_{m2} value after adding TiB_2-based fillers. The changes in T_m values also signify the interfacial interaction between fillers and PU, which is attributed to the reduced molecular motion of PU chains. Additionally, we calculated the % crystallinity (χ_c) and found that neat PU and composites remain mostly amorphous (Table S6†). In simulation, we built our PU model as amorphous using this information.

The work reported here presents a systematic investigation of the candidacy of TiB_2-based fillers in reinforcing the mechanical properties of a polymer. This study highlights that reinforcing of the mechanical properties of a polymer depends on the filler geometry, filler–matrix interphase, and Young's modulus of the fillers itself as explained below.[69]

Filler geometry and filler–matrix interaction. We found that p-NS-based composites demonstrated better mechanical performance than b-TiB_2-based composites, which is attributed to the 2D geometry of the p-NS, facilitating a more effective stress transfer than three-dimensional b-TiB_2. However, f-NS, despite having the 2D geometry, lead to only nominal enhancement in the mechanical performance of PU. This is attributed to their incompatibility with the base polymer and the distorted crystal lattice, which affects the strength of the interphase. As we know, if the filler–polymer interphase is not strong enough to withstand the applied stress, it results in poor stress transfer.

Young's modulus of fillers. The improvement in the mechanical properties of composites also depends upon the intrinsic mechanical properties of fillers, which are primarily measured using Young's modulus. If the modulus of fillers is high compared with the polymer, shear stress would be induced at the filler/PU interphase. Consequently, the filler would bear most of the applied stress, resulting in better mechanical properties. We observed an improvement in the mechanical properties of the b-TiB_2/PU composite despite it having a three-dimensional geometry (although it was lower than that of the p-NS/PU composite). The improvement in the mechanical properties of b-TiB_2 is also because of the high Young's modulus, ~565 GPa.[34] Such a high value of Young's modulus is attributed to the unique graphenic arrangement of boron atoms in between the titanium metal, as shown in Fig. S14, ESI.†[70] However, Young's modulus of nanosheets synthesized from b-TiB_2 has not been reported so far. Still, we can assume that if their intrinsic graphenic arrangement remained intact during nanoscaling, the modulus would increase significantly, similar to that for graphene.[71] This assumption aligns with the observed enhancement in the mechanical properties of p-NS/PU composites – with p-NS being the 2D counterpart of b-TiB_2, in which the native lattice of TiB_2 is retained to a large extent. However, during the synthesis of f-NS, the chemical synthesis route distorts the native lattice of TiB_2, which probably caused a decrease in Young's modulus of these nanosheets. This is also one of the reasons behind the decrease in the overall mechanical response of f-NS/PU composites.

Conclusions

To sum up, we demonstrate that quasi-2D nanostructures from TiB_2 can lead to a significant enhancement in the mechanical properties of polyurethane, even at low-weight fractions. We show that an enhancement of up to ~80% in the UTS and toughness can be obtained by adding pristine nanosheets of TiB_2 to PU. A *vis-à-vis* comparison of composites prepared using functionalized nanosheets of TiB_2 indicates that this enhancement is closely linked to the nature of the interphase formed between the PU matrix and TiB_2 nanofillers. We acknowledge that certain trade-offs are associated with the addition of TiB_2-based fillers. While all TiB_2-based fillers are found to improve the tensile strength of PU, the b-TiB_2 and f-NS fillers are associated with a more pronounced reduction in flexibility compared with the p-NS filler. Additionally, while b-TiB_2 and p-NS improved thermal stability, the inclusion of f-NS adversely affects the thermal stability, highlighting the critical role of the native metal boride lattice in determining the composite performance. We also obtained computational insights to understand how nano-scaled TiB_2 fillers endow superior mechanical properties to the PU matrix. Simulations reveal that TiB_2 nanosheets not only actively contribute to load distribution but also promote isotropic mechanical behaviour. This study highlights the potential of TiB_2-based nanofillers in reinforcing polymer matrices. We also showcase how hydrogen bonding varies with the inclusion of different variants of TiB_2-based fillers within the PU matrix. It would be promising to explore temperature-dependent changes in hydrogen bonding in these composite films. The multi-functional nature of TiB_2-based nanosheets makes such composites useful for diverse applications such as flexible electronics, energy storage systems, and medical devices.

Methods

Synthesis of TiB_2-derived pristine nanosheets

TiB_2-derived pristine nanosheets (p-NS) were synthesized as reported in our recent work[30] using high-energy ball milling (Dual Mixer/Mill 8000D from SPEX SamplePrep). In a single batch, ~1.3 g of TiB_2 powder (Sigma-Aldrich, 99.5% pure, particle size <10 μm) was added to a zirconia vial (ZrO_2) along with ZrO_2 balls in order to maintain a 20 : 1 ball-to-powder ratio (BPR). After adding the balls and TiB_2 powder, the vial was sealed with an O-ring to prevent the loss of material during the milling process. After that, the vial was loaded into the mill. One more empty vial was loaded in the opposite slot of the ball mill to maintain equal weights at both ends. The run was performed for 6 h to achieve complete exfoliation. After completion of the run, the milled powder comprising nanosheets was scrapped from the vial and stored in a desiccator.

Synthesis of functionalized TiB_2 nanosheets

TiB_2-derived functionalized nanosheets (f-NS) were synthesized using the dissolution and recrystallization approach as reported previously by our group.[32] Briefly, 300 mg of TiB_2 powder (Sigma Aldrich, 99.5% pure, size <10 μm) was added to 90 mL of deionized water and stirred at 250 rpm for 10 minutes to form a black suspension. Then, in this black suspension, 10 mL of hydrogen peroxide (H_2O_2) (Merck, 30%) was added dropwise. After continuous stirring for 1 h, the suspension gradually turned yellow in color. The suspension was

left undisturbed for 24 h, after which the yellow top phase was collected and centrifuged at 8000 rpm for 30 minutes at 20 °C. After centrifugation, the supernatant was collected and frozen at −4 °C for 24 h. This frozen sample was subsequently lyophilized (Martin Christ Alpha-2D Plus) for 72 hours, which resulted in a pale-yellow fluffy powder comprising functionalized nanosheets.

Preparation of polymer composites using TiB_2-based fillers

Polyurethane (PU) composites with different wt% of TiB_2-based fillers were prepared using the solution casting method. In the first step, PU beads (Estane® 5707 TPU, refer Section 17, ESI, for more details†) were dissolved in dimethyl formamide (DMF) (Emplura, 99% pure) by stirring them at 150 rpm for 3 h at 80 °C to obtain a 75 mg ml^{-1} polymer stock solution. In the second step, TiB_2-based fillers (at different wt% – 0.5%, 1%, 1.5%, 2%, and 5%) were dispersed in an appropriate amount of PU stock solution and DMF solvent. The amount of each component was adjusted such that the final dispersions have the same weight and same volume (600 mg and 30 mL, as explained in Table S7 in the ESI†). These dispersions were obtained by stirring at 250 rpm for 5 min, followed by bath sonication for 1 min. In the third step, this dispersion was poured into glass Petri dishes, placed in a vacuum oven, and dried at 60 °C for 96 h to evaporate the solvent. In the final step, the dried composites were allowed to cool at room temperature, following which the films were carefully peeled off using tweezers, as shown in Fig. 1(a–f). We used three types of TiB_2 fillers for the preparation of the TiB_2/PU composite. By following the same procedure, we prepared triplicate of each sample for further analysis.

Tensile testing of composite films

After peeling off the films, the samples were cut into rectangular specimens measuring 2.5 cm × 6 cm. These rectangular test specimens were clamped in a Universal Testing Machine (UTM) (NTF computerized tensile strength tester) for tensile testing. After clamping, a specimen was stretched at a constant crosshead speed of 100 mm min^{-1}. The stress and strain values were calculated using the following expressions.

$$\text{Stress} = \frac{\text{Load}}{\text{Cross-sectional area}} \quad (1)$$

$$\text{Strain} = \frac{\text{Displaced length}}{\text{Original length}} \quad (2)$$

Young's modulus was calculated by selecting the linear region of the stress–strain plot. Selected data points from the linear region were replotted and fitted using a linear fit function in Origin software. The slope of the linear fit corresponds to Young's modulus. For each type of sample, at least three samples were tested to ensure the accuracy of the measured properties. We expressed all the mechanical properties as mean ± standard deviation.

Field emission scanning electron microscopy (FE-SEM)

Field emission scanning electron microscopy (FE-SEM) images of fillers and composite films before and after fracture were captured using a JEOL JSM 7600F instrument. The instrument was operated at 3 kV with a working distance of 8 mm. For imaging, the powder sample was dusted on carbon tape, while composite films were directly used after being cut into 0.5 cm × 0.5 dimensions. After mounting on SEM stubs, the samples were coated with platinum for about 80 s.

Transmission electron microscopy (TEM)

Transmission electron microscopy (TEM) images of nanofillers and composite films were obtained using a Thermo Scientific Themis 300 instrument operating at 300 kV. For imaging TiB_2 fillers, the samples were prepared as follows—1 mg mL^{-1} suspension of the powder form of nanosheets in DI water was prepared using bath sonication for 10 min (Bandelin Sonorex Digitec, 140 W, 35 kHz). This suspension was further diluted 100×, and from that, 15 μL of this diluted suspension was drop cast onto lacey carbon Cu grids (Ted Pella, 300 mesh). For imaging the nanocomposite, ultra-thin sections (less than 100 nm) of the composite film embedded in epoxy were prepared using an ultramicrotome (Leica, Ultracut EM FC6). These ultra-thin sections were transferred onto the lacey carbon Cu grids (Ted Pella, 300 mesh). The obtained images were further processed using GATAN software.

Atomic force microscopy (AFM)

Atomic force microscopy (AFM) images of nanofillers were obtained using a Bruker NanoWizard Sense AFM instrument operated in the tapping mode using a Sb-doped silica cantilever (spring constant = 3 N m^{-1}, resonant frequency = 75 kHz). Briefly, 1 mg mL^{-1} suspension of the powder form of nanosheets in DI water was prepared using bath sonication for 10 min (Bandelin Sonorex Digitec, 140 W, 35 kHz). This suspension was diluted 200×, and 10 μL of that diluted suspension was drop-cast on a freshly cleaved mica substrate followed by drying in a desiccator for 24 h. The obtained images were processed using JPK NanoWizard Sense + software.

Fourier-transform infrared spectroscopy (FTIR)

Fourier transform infrared spectroscopy (FTIR) of TiB_2-based fillers and composite films was performed using a Spectrum Two, PerkinElmer instrument. The scanning was performed in the range of 400 to 4000 cm^{-1}.

X-ray diffraction (XRD)

X-ray diffraction (XRD) analysis of TiB_2-based fillers was performed using a D8 DISCOVER (Bruker) instrument, whereas a multipurpose X-ray diffractometer (SmartLab, Rigaku Corp., Japan) was used to measure composite films using Cu Kα-radiation (λ = 1.54 Å). For the analysis, the scan range was set from 5° to 90° (in 2θ). After collecting the data, we analyzed the data using an ICDD data file-TiB_2: 00-351-0741.

X-ray photoelectron spectroscopy (XPS)

X-ray photoelectron spectroscopy (XPS) data of the composite film were recorded using a Thermofisher Scientific Nexsa base model using monochromatic Al Kα as a source with 1486.6 eV energy. Recorded data were baseline corrected and deconvoluted using origin software.

Thermal behaviour analysis

Thermogravimetric analysis (TGA) of composite films was performed using a PerkinElmer TGA system, and differential scanning calorimetry (DSC) analysis of composite films was conducted using a TA-instruments DSC 5000 system. For TGA, the temperature was varied from 30 °C to 800 °C with a nitrogen (N_2) flow rate of 10 mL min^{-1}. The initial weight of the sample for TGA was ~2 mg. For DSC, the temperature was varied from −70 °C to 150 °C with a N_2 flow rate of 10 mL min^{-1}. The initial weight of the sample for DSC was ~10 mg.

Dynamic mechanical analysis (DMA)

Dynamic mechanical analysis (DMA) of the composite film was performed using a TA-instruments DMA 850. The temperature was varied from −70 °C to 150 °C with a heating rate of 5 °C min^{-1} at a constant vibrational frequency of 1 Hz. The sample dimensions for the analysis were 3.5 cm × 0.6 cm.

Model construction and simulation

For molecular dynamics simulations of the composite, the initial simulation setup comprising multiple PU chains was modeled using the MedeA simulation package.[72] Energy minimization was carried out on a large simulation cell that contained sufficient spacing between the PU chains. All interactions between the chains were described using the recent version of the polymer consistent force field (*pcff*+), which includes detailed parameters for bonded interactions (bond stretching, angle bending and dihedral interactions) and non-bonded interactions (van der Waals and electrostatic forces). The information on the functional form of the *pcff*+ force field is mentioned in Section S19, ESI.† The PU chains modeled in this study consisted of four hard segments (MDI/BDO) at either end, and 24 soft segments (PTMO) in the center, maintaining a hard-to-soft segment ratio of 1 : 3. To elucidate the atomistic deformation mechanisms and highlight the qualitative variation of the mechanical behavior as observed in our experiments, we consider neat PU and nanosheets of TiB_2 as reinforcement in TiB_2-NS/PU composites with varying weight fractions of the nanosheets. Fully periodic (bulk) models of neat PU and TiB_2-NS/PU composites were developed and subjected to tensile testing using the LAMMPS (Large-scale Atomic/Molecular Massively Parallel Simulator) simulation package.[73]

All systems consisted of a total of 256 PU chains comprising 127 656 atoms. The amorphous PU matrix was generated by heating the system to 800 K for 300 ps using the Nosé–Hoover thermostat and barostat, well above its glass transition temperature. The system was then cooled to room temperature (300 K) at a rate of 1 K ps^{-1} and equilibrated under anisotropic NPT conditions at 300 K and 1 atm for 2 ns to achieve the target density of 0.91 g cm^{-3}. Tensile deformation was carried out on the equilibrated systems at a strain rate of 10^9 s^{-1}, up to a total strain of 900%. The TiB_2-NS were modeled with an aspect ratio of 1 : 4, based on an 8 × 8 × 2 TiB_2 supercell derived from the unit cell of TiB_2 provided in the Materials Project database.[74] (Here the1 : 4 aspect ratio is taken as per the value reported in the literature[30] for TiB_2-based nanosheets.) We employed the modified embedded atom method (MEAM) potential to model the pairwise interactions of TiB_2.[75] Cross-interaction parameters between the polymer and TiB_2 were defined using Lennard-Jones (LJ) parameters and the Lorentz–Berthelot mixing rule. The LJ parameters for Ti and B atoms taken for the cross interactions with PU were those from the MEAM potential.

The equilibration protocol for the composites followed a similar protocol to that of the neat PU (heating to 800 K and subsequently cooling to 300 K to generate an amorphous PU matrix with embedded TiB_2 nanosheets). Following anisotropic equilibration under NPT, tensile testing was conducted at a strain rate of 10^9 s^{-1} until failure.

Data availability

The data supporting this article have been included as part of the ESI.†

Conflicts of interest

The authors declare no conflicts of interest.

Acknowledgements

We sincerely acknowledge the Central Instrumentation Facility (CIF) at IIT Gandhinagar for providing access to various instruments that were essential for our characterization work. We also extend our gratitude to CRF-IIT Delhi for facilitating TEM, DSC, and DMA analyses and to AMRC-IIT Mandi for supporting us with XPS analysis. K. J. acknowledges the funding received from the seed grant IITGN, the Core Research Grant (No. CRG/2023/008191) awarded by SERB India, the STARS Research Grant (No. MoE-STARS/STARS-2/2023-1024) of the Ministry of Education, India, and the financial support from the Dr Dinesh O. Shah Chair Fellowship. We also acknowledge the Department of Scientific and Industrial Research (DSIR) for enabling the use of the Common Research & Technological Development Hub (CRTDH) facility (Grant DSIR/CRTDH/NM/IIT-Gn/2016), and the DST-FIST grant [SR/FST/ET-I/2020/554]. R. R. acknowledges the supercomputing facility of IIT Gandhinagar (Param Ananta) and NIT Trichy (Param Porul) for all the simulations and funding support from the Core Research Grant (No. CRG/2023/005333). The authors wish to especially thank Dr Krishna Kanti Dey for kindly allowing us to

use the vacuum oven, Dr Abhijit Mishra and his student Prathmesh Bhadane for their assistance with the UTM, and Anshul Rasyotra for his valuable insights into designing the experiments. We also want to thank our Chemical Department office staff members – Mr Suvakanta, Mr Rajib, Mr Supresh, and Mr Rohit – for their prompt assistance in procuring chemicals and instruments.

References

1 K. S. Novoselov, A. K. Geim, S. V. Morozov, D. Jiang, Y. Zhang, S. V. Dubonos, I. V. Grigorieva and A. A. Firsov, *Science*, 2004, **306**, 666–669.
2 A. K. Geim and K. S. Novoselov, *Nat. Mater.*, 2007, **63**(6), 183–191.
3 S. Z. Butler, S. M. Hollen, L. Cao, Y. Cui, J. A. Gupta, H. R. Gutiérrez, T. F. Heinz, S. S. Hong, J. Huang, A. F. Ismach, E. Johnston-Halperin, M. Kuno, V. V. Plashnitsa, R. D. Robinson, R. S. Ruoff, S. Salahuddin, J. Shan, L. Shi, M. G. Spencer, M. Terrones, W. Windl and J. E. Goldberger, *ACS Nano*, 2013, **7**(4), 2898–2926.
4 A. Rasyotra, A. Thakur, B. Gaykwad, S. Chakrabarty, I. Bayad, J. Parikh and K. Jasuja, *J. Mater. Sci.*, 2023, **58**, 4359–4383.
5 V. Shanmugam, R. A. Mensah, K. Babu, S. Gawusu, A. Chanda, Y. Tu, R. E. Neisiany, M. Försth, G. Sas and O. Das, *Part. Part. Syst. Charact.*, 2022, **39**, 2200031.
6 R. L. D. Whitby, *ACS Nano*, 2014, **8**, 9733–9754.
7 Z. Yuan, X. Xiao, J. Li, Z. Zhao, D. Yu and Q. Li, *Adv. Sci.*, 2018, **5**, 1700626.
8 S. Zhao, M. Li, X. Wu, S. H. Yu, W. Zhang, J. Luo, J. Wang, Y. Geng, Q. Gou and K. Sun, *Mater. Today Adv.*, 2020, **6**, 100060.
9 J. Hu, S. Zhang and B. Tang, *Energy Storage Mater.*, 2021, **34**, 260–281.
10 S. Bera, M. Singh, R. Thantirige, S. K. Tiwary, B. T. Shook, E. Nieves, D. Raghavan, A. Karim and N. R. Pradhan, *Small Sci.*, 2023, **3**, 2300016.
11 A. Qadir, T. K. Le, M. Malik, K. A. A. Min-Dianey, I. Saeed, Y. Yu, J. R. Choi, P. V. Pham, S. K. Krishnan, E. Singh, P. Singh, M. Meyyappan and H. S. Nalwa, *RSC Adv.*, 2021, **11**, 23860–23880.
12 S. K. Krishnan, E. Singh, P. Singh, M. Meyyappan and H. S. Nalwa, *RSC Adv.*, 2019, **9**, 8778–8881.
13 L. Ji, P. Meduri, V. Agubra, X. Xiao and M. Alcoutlabi, *Adv. Energy Mater.*, 2016, **6**, 1502159.
14 H. E. Karahan, K. Goh, C. (John) Zhang, E. Yang, C. Yıldırım, C. Y. Chuah, M. G. Ahunbay, J. Lee, Ş. B Tantekin-Ersolmaz, Y. Chen and T.-H. Bae, *Adv. Mater.*, 2020, **32**, 1906697.
15 X. Sun, C. Huang, L. Wang, L. Liang, Y. Cheng, W. Fei and Y. Li, *Adv. Mater.*, 2021, **33**, 2001105.
16 M. G. Rasul, A. Kiziltas, B. Arfaei and R. Shahbazian-Yassar, *npj 2D Mater. Appl.*, 2021, **5**, 56.
17 H. Kim, A. A. Abdala and C. W. Macosko, *Macromolecules*, 2010, **43**, 6515–6530.
18 X. Wang, Y. Hu, L. Song, H. Yang, W. Xing and H. Lu, *J. Mater. Chem.*, 2011, **21**, 4222–4227.
19 W. Cai, X. Mu, Y. Pan, W. Guo, J. Wang, B. Yuan, X. Feng, Q. Tai and Y. Hu, *Polym. Adv. Technol.*, 2018, **29**, 2545–2552.
20 X. Wang, E. N. Kalali and D.-Y. Wang, *J. Mater. Chem. A*, 2015, **3**, 24112–24120.
21 H. Riazi, S. K. Nemani, M. C. Grady, B. Anasori and M. Soroush, *J. Mater. Chem. A*, 2021, **9**, 8051–8098.
22 X. Sheng, Y. Zhao, L. Zhang and X. Lu, *Compos. Sci. Technol.*, 2019, **181**, 107710.
23 S. Habibpour, K. Zarshenas, M. Zhang, M. Hamidinejad, L. Ma, C. B. Park and A. Yu, *ACS Appl. Mater. Interfaces*, 2022, **14**, 21521–21534.
24 S. Chakrabarty, A. Thakur, A. Rasyotra, B. Gaykwad and K. Jasuja, *J. Phys. Chem. C*, 2023, **127**, 852–870.
25 S. K. Das and K. Jasuja, *ACS Appl. Nano Mater.*, 2018, **1**, 1612–1622.
26 S. K. Das, A. Bedar, A. Kannan and K. Jasuja, *Sci. Rep.*, 2015, **5**, 10522.
27 A. L. James and K. Jasuja, *RSC Adv.*, 2017, **7**, 1905–1914.
28 A. Yousaf, M. S. Gilliam, S. L. Y. Chang, M. Augustin, Y. Guo, F. Tahir, M. Wang, A. Schwindt, X. S. Chu, D. O. Li, S. Kale, A. Debnath, Y. Liu, M. D. Green, E. J. G. Santos, A. A. Green and Q. H. Wang, *J. Phys. Chem. C*, 2021, **125**, 6787–6799.
29 A. Rasyotra, A. Thakur, S. Shukla, R. Mandalia, R. Ranganathan and K. Jasuja, *ACS Sustainable Chem. Eng.*, 2025, **13**(6), 2312–2323.
30 B. Gaykwad, A. Thakur, A. Buch and K. Jasuja, *J. Phys. Chem. C*, 2023, **127**(32), 15887–15900.
31 A. Rasyotra, A. Thakur, R. Mandalia, R. Ranganathan and K. Jasuja, *Nanoscale*, 2023, **15**, 8204–8216.
32 A. L. James, M. Lenka, N. Pandey, A. Ojha, A. Kumar, R. Saraswat, P. Thareja, V. Krishnan and K. Jasuja, *Nanoscale*, 2020, **12**, 17121–17131.
33 Z. Li, B. Zhao, L. Wang, Q. Tao and P. Zhu, *J. Phys.: Condens. Matter*, 2023, **35**, 074002.
34 R. G. Munro, *J. Res. Natl. Inst. Stand. Technol.*, 2000, **105**, 709.
35 E. Solfiti and F. Berto, *Procedia Struct. Integr.*, 2020, **25**, 420–429.
36 J. Xiao, L. Zhang, K. Zhou, J. Li, X. Xie and Z. Li, *Carbon*, 2013, **65**, 53–62.
37 M. Wang, D. Chen, Z. Chen, Y. Wu, F. Wang, N. Ma and H. Wang, *Mater. Sci. Eng., A*, 2014, **590**, 246–254.
38 M. K. Akbari, H. Baharvandi and K. Shirvanimoghaddam, *Mater. Des.*, 2015, **66**, 150–161.
39 S. Venkatesan, J. Jerald, D. Sundeep, E. K. Varadharaj and C. C. Sastry, *Surf. Topogr.:Metrol. Prop.*, 2022, **10**, 35003.
40 S. K. John and A. A. Anappara, *New J. Chem.*, 2019, **43**, 9953–9960.
41 R. Patidar, H. Gunda, A. K. Varma, R. Gawas, S. K. Das and K. Jasuja, *Ceram. Int.*, 2020, **46**, 28324–28331.

42 F. M. de Souza, P. K. Kahol and R. K. Gupta, in *Polyurethane Chemistry: Renewable Polyols and Isocyanates*, American Chemical Society, 2021, vol. 1380, pp. 1.
43 U. Khan, P. May, A. O'Neill and J. N. Coleman, *Carbon*, 2010, **48**, 4035–4041.
44 H. Li, J.-T. Sun, C. Wang, S. Liu, D. Yuan, X. Zhou, J. Tan, L. Stubbs and C. He, *ACS Sustainable Chem. Eng.*, 2017, **5**, 7942–7949.
45 A. Pei, J.-M. Malho, J. Ruokolainen, Q. Zhou and L. A. Berglund, *Macromolecules*, 2011, **44**, 4422–4427.
46 X. Dai, J. Xu, X. Guo, Y. Lu, D. Shen, N. Zhao, X. Luo and X. Zhang, *Macromolecules*, 2004, **37**, 5615–5623.
47 S. L. Phua, L. Yang, C. L. Toh, S. Huang, Z. Tsakadze, S. K. Lau, Y.-W. Mai and X. Lu, *ACS Appl. Mater. Interfaces*, 2012, **4**, 4571–4578.
48 S. Benli, Ü. Yilmazer, F. Pekel and S. Özkar, *J. Appl. Polym. Sci.*, 1998, **68**, 1057–1065.
49 P. A. Gunatillake, G. F. Meijs, S. J. Mccarthy and R. Adhikari, *J. Appl. Polym. Sci.*, 2000, **76**, 2026–2040.
50 B. Fernández-d'Arlas, R. P. Baumann, E. Pöselt and A. J. Müller, *CrystEngComm*, 2017, **19**, 4720–4733.
51 H. Zhang, L. Wang, Q. Chen, P. Li, A. Zhou, X. Cao and Q. Hu, *Mater. Des.*, 2016, **92**, 682–689.
52 Z. Li, M. Liu and R. J. Young, *Nano Mater. Sci.*, 2024, DOI: **10.1016/j.nanoms.2024.04.014**.
53 U. Khan, P. May, A. O'Neill, A. P. Bell, E. Boussac, A. Martin, J. Semple and J. N. Coleman, *Nanoscale*, 2013, **5**, 581–587.
54 M. Majdoub, Y. Essamlali, O. Amadine, I. Ganetri and M. Zahouily, *New J. Chem.*, 2019, **43**, 15659–15672.
55 S. Thakur and N. Karak, *RSC Adv.*, 2013, **3**, 9476–9482.
56 C. Xiang, P. J. Cox, A. Kukovecz, B. Genorio, D. P. Hashim, Z. Yan, Z. Peng, C.-C. Hwang, G. Ruan, E. L. G. Samuel, P. M. Sudeep, Z. Konya, R. Vajtai, P. M. Ajayan and J. M. Tour, *ACS Nano*, 2013, **7**, 10380–10386.
57 Y. Liu, N. Wu, S. Zheng, Y. Yang, B. Li, W. Liu, J. Liu and Z. Zeng, *ACS Appl. Mater. Interfaces*, 2022, **14**, 50120–50128.
58 T. Wu and B. Chen, *Sci. Rep.*, 2017, **7**, 17470.
59 C. Cazan, A. Enesca and L. Andronic, *Polymers*, 2021, **13**, 2017.
60 N. Lempesis, P. J. in't Veld and G. C. Rutledge, *Macromolecules*, 2017, **50**, 7399–7409.
61 S. Zhu, N. Lempesis, P. J. in't Veld and G. C. Rutledge, *Macromolecules*, 2018, **51**, 1850–1864.
62 A. Talapatra and D. Datta, *Mol. Simul.*, 2021, **47**, 602–618.
63 J. Koyanagi, N. Takase, K. Mori and T. Sakai, *Compos., Part C: Open Access*, 2020, **2**, 100041.
64 S. Mandal, D. Roy, K. Mukhopadhyay, M. Dwivedi and M. Joshi, *RSC Appl. Interfaces*, 2024, **1**, 977–991.
65 A. Kumawat, K. Jasuja and C. Ghoroi, *ACS Appl. Bio Mater.*, 2023, **6**, 4111–4126.
66 A. Niemczyk, A. Piegat, Á. S. Olalla and M. El Fray, *Eur. Polym. J.*, 2017, **93**, 182–191.
67 A. K. Barick and D. K. Tripathy, *Mater. Sci. Eng., B*, 2011, **176**, 1435–1447.
68 X. Li, H. Deng, Z. Li, H. Xiu, X. Qi, Q. Zhang, K. Wang, F. Chen and Q. Fu, *Composites, Part A*, 2015, **68**, 264–275.
69 R. J. Young, M. Liu, I. A. Kinloch, S. Li, X. Zhao, C. Vallés and D. G. Papageorgiou, *Compos. Sci. Technol.*, 2018, **154**, 110–116.
70 X. Lv, Z. Yin, Z. Yang, J. Chen, S. Zhang, S. Song and G. Yu, *Prog. Mater.*, 2024, **6**, 9.
71 C. Lee, X. Wei, J. W. Kysar and J. Hone, *Science*, 2008, **321**, 385–388.
72 A. Jain, S. P. Ong, G. Hautier, W. Chen, W. D. Richards, S. Dacek, S. Cholia, D. Gunter, D. Skinner, G. Ceder and K. A. Persson, *APL Mater.*, 2013, **1**, 11002.
73 A. P. Thompson, H. M. Aktulga, R. Berger, D. S. Bolintineanu, W. M. Brown, P. S. Crozier, P. J. in't Veld, A. Kohlmeyer, S. G. Moore, T. D. Nguyen, R. Shan, M. J. Stevens, J. Tranchida, C. Trott and S. J. Plimpton, *Comput. Phys. Commun.*, 2022, **271**, 108171.
74 A. Stukowski, *Model. Simul. Mater. Sci. Eng.*, 2010, **18**, 15012.
75 S. Attarian and S. Xiao, *Comput. Mater. Sci.*, 2022, **201**, 110875.